

On the self-similarity of line segments in decaying homogeneous isotropic turbulence

Michael Gauding^{a,*}, Lipo Wang^b, Jens Henrik Goebbert^c, Mathis Bode^d,
Luminita Danaila^a, Emilien Varea^a

^a*CORIA – CNRS UMR 6614, Saint Etienne du Rouvray, France*

^b*UM-SJTU Joint Institute, Shanghai JiaoTong University, Shanghai, China*

^c*Juelich Supercomputing Center, Juelich, Germany*

^d*Institute for Combustion Technology, RWTH Aachen University, Germany*

Abstract

The self-similarity of a passive scalar in homogeneous isotropic decaying turbulence is investigated by the method of line segments (M. Gauding et al., *Physics of Fluids* 27.9 (2015): 095102). The analysis is based on a highly resolved direct numerical simulation of decaying turbulence. The method of line segments is used to perform a decomposition of the scalar field into smaller sub-units based on the extremal points of the scalar along a straight line. These sub-units (the so-called line segments) are parameterized by their length ℓ and the difference $\Delta\phi$ of the scalar field between the ending points. Line segments can be understood as thin local convective-diffusive structures in which diffusive processes are enhanced by compressive strain. From DNS, it is shown that the marginal distribution function of the length ℓ assumes complete self-similarity when re-scaled by the mean length ℓ_m . The joint statistics of $\Delta\phi$ and ℓ , from which the local gradient $g = \Delta\phi/\ell$ can be defined, play an important role in understanding the turbulence mixing and flow structure. Large values of g occur at a small but finite length scale. Statistics of g are characterized by rare but strong deviations that exceed the standard deviation by more than one order of magnitude. It is shown that these events break complete self-similarity of line segments, which confirms the standard paradigm of turbulence that intense events (which are known as internal intermittency) are not self-similar.

*Corresponding author

Email address: michael.gauding@coria.fr (Michael Gauding)

1. Introduction

The turbulent motion of fluids is a highly complex phenomenon. In general, turbulent flows are characterized by random spatio-temporal fluctuations over a broad range of scales. Reliable predictions of the statistical properties of these fluctuations will be of practical importance for a wide field of applications.

Historically, turbulence research has mostly focused on a statistical description in the sense of Kolmogorov's scaling theory [24, 25], which hypothesizes that for sufficiently large Reynolds numbers, the small scale motion is statistically independent from the large scales. While the large scales depend on the boundary or initial conditions, the smallest scales should be statistically universal and feature certain symmetries that are recovered in a statistical sense. Following Kolmogorov's theory, the small scales can be uniquely described by simple parameters such as the kinematic viscosity ν of the fluid and the mean dissipation rate. However, numerous experimental and numerical studies have reported a substantial deviation from Kolmogorov's prediction [13, 45]. The turbulent fluid motion is extremely fluctuating and the intensity of these fluctuations increases strikingly with increasing Reynolds number or decreasing scale. This phenomenon is referred to as internal intermittency. Nelkin [29] claimed that the origin of intermittency lies in the non-linear and non-local vortex stretching mechanism. The consequence of internal intermittency is the break-down of small-scale universality, which dramatically complicates theoretical approaches from first principles. Even for the most canonical flows, such as homogeneous isotropic turbulence, no closed theory for intermittency exists [32].

It is customary to investigate the statistical structure of turbulence by means of velocity or scalar increments over a given range of scales. The scalar can be either concentration or temperature, provided that buoyancy effects are negligible. Kolmogorov's scaling theory has been generalized to scalar fields by Obukhov [30] and Corrsin [8] (referred to as KOC-theory in the following). The moments of the increments are known as structure functions. Transport equations for the structure functions have been first derived by Kolmogorov [24] for the velocity field and by Yaglom [59] for a scalar field. Physically, structure functions provide an information about the energy at a given length-scale r and all smaller scales [11]. In other words, structure functions at scale r are contaminated with information coming from all smaller length-scales. Spectral representations have the same deficiency, as structure functions and energy spectra are related by an integral transformation. Moreover, by defining structure functions over a

given scale r , the information of the length-scale distribution of the turbulent field is lost after applying an ensemble-average operation.

The concept of self-similarity is less strict than universality and has been one of the key elements in shaping our understanding of turbulent flows [17, 42]. The self-similarity hypotheses was first put forward by von Karman and Howarth [50] for the correlation functions of the velocity and afterwards, several other problems in turbulence research have been approached in this framework [2, 10, 12, 48]. The assumption of self-similarity imposes certain constraints on the dynamics of the flow. In particular, complete self-similarity requires that all statistics, such as structure functions or correlation functions, can be expressed by functional forms. For instance, the second-order scalar structure function $\langle(\delta\phi)^2\rangle$ can be written as

$$\langle(\delta\phi)^2\rangle = A(t)f(\tilde{r}), \quad (1)$$

where the pre-factor $A(t)$ depends solely on time, while the normalized shape function $f(\tilde{r})$ depends solely on the normalized separation distance \tilde{r} , with $\tilde{r} = r/L(t)$, and $L(t)$ being a single characteristic length-scale. However, many flows do not satisfy complete self-similarity [28]. The term partial self-similarity refers to flows in which self-similarity is valid for a restricted range of scales only, requiring at least two different length-scales to describe statistical quantities. Determining these scales and its scaling is of high relevance for understanding and modeling turbulence.

A novel statistical approach to investigate the local structure of turbulence was proposed by Wang and Peters [55, 56] by exploiting the topological features of local extremal points in turbulent fields. The motivation behind this approach is the fact that the extremal points inherit physics from the dynamics of turbulence: fluctuations disturb the turbulent field and create new extremal points, while diffusion will smooth the field and annihilate the extremal points. Strain acting on the turbulent field does not change the number of extremal points but can move the position of the extremal points relatively to each other. The extremal points can be considered within different frameworks, such as along straight lines [16], gradient trajectories [55], stream lines [53], vortex lines [57], and Lagrangian trajectory paths [54]. Recently, statistics of extremal points have been studied in the context of turbulent combustion [7, 15] and within a framework to predict local detonation events in super-charged spark-ignition engines [33].

In this work, we adopt the approach of Gauding et al. [16] to analyze turbulent scalar mixing in decaying homogeneous isotropic turbulence. The turbulent signal of the passive scalar $\phi(\boldsymbol{x}, t)$ is decomposed along a straight

line into piece-wise monotonously increasing or decreasing segments. These so-called line segments start at a local minimum point of the scalar field and end at a local maximum point of the scalar field or vice versa. By this definition, line segments can be parameterized by the distance $\ell = x_{\text{end}} - x_{\text{start}}$ and the scalar difference $\Delta\phi = \phi(x_{\text{end}}) - \phi(x_{\text{start}})$ between the end and start point. This concept is demonstrated in fig. 1. Depending on the sign of $\Delta\phi$, there are positive (increasing) or negative (decreasing) segments. The decomposition by line segments is self-contained and has the properties of completeness and uniqueness meaning that each material point is included once and only once in the decomposed object.

Such decomposition is physically meaningful in the following sense. By decomposing the turbulent field into space-filling sub-units, the properties of the entire field can be reproduced from the statistics of the relatively simple sub-units. In this sense, the complexity of the problem will be reduced. Specifically, suppose the sub-units can be characterized by a set of representative parameters (p_1, \dots, p_n) . In principle it will be much more challenging to parameterize a turbulent quantity X for the entire field than to parameterize X with (p_1, \dots, p_n) for each individual sub-unit because of the relatively simple sub-unit structure. When the joint probability density function $P(p_1, \dots, p_n)$ of the parameter set p_i is known, the ensemble average of X is determined as

$$\langle X \rangle = \int \dots \int X(p_1, \dots, p_n) P(p_1, \dots, p_n) dp_1 \dots dp_n. \quad (2)$$

It is worthy noting that eq. (2) for reconstructing X is valid if and only if the sub-units are space-filling.

Finally, we want to emphasize the difference between the scalar difference $\Delta\phi$ of line segments and the increment $\delta\phi = \phi(\mathbf{x} + \mathbf{r}) - \phi(\mathbf{x})$ used in classical theories. The increment $\delta\phi$ is computed continuously along a straight line and the separation distance r between the two points is imposed externally. For line segments, the length-scale ℓ results from the turbulent field itself, rather than being prescribed externally, and the scalar difference $\Delta\phi$ is conditioned on local extremal points. This approach is therefore capable to characterize the local structure of turbulence.

The objective of this study is to use the concept of line segments to analyze scalar mixing in decaying homogeneous isotropic turbulence. The remainder of the paper is as follows. In sec. 2 we present the direct numerical simulations (DNS) on which the analysis is based. In sec. 3 we discuss the length distribution of line segments and motivate the scaling of the mean length by using a statistical approach. Joint statistics of $\Delta\phi$ and ℓ and their

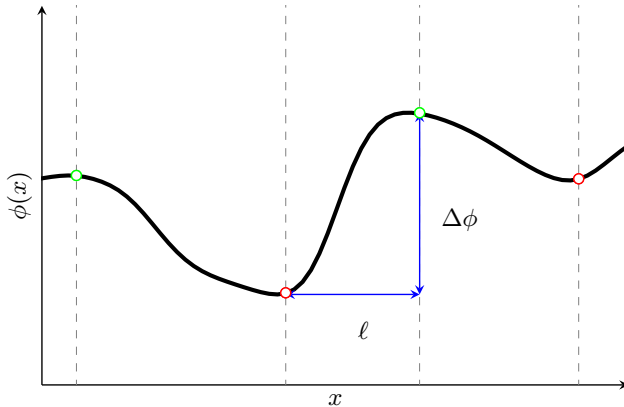


Figure 1: Illustration of the parameterization of line segments by $\Delta\phi$ and ℓ for a signal $\phi(x)$. Line segments are bounded by adjacent local minimum and maximum points, which are indicated by red and green circles, respectively.

self-similarity are presented in sec. 4. Conditional averages of these quantities are presented in sec. 5. The statistics are discussed from a self-similarity perspective. We identify quantities that satisfy complete self-similarity, such as the distribution of the length ℓ , and quantities that reveal only partial self-similarity, such as the joint distribution of $\Delta\phi$ and ℓ . We conclude the paper in sec. 6.

2. Direct numerical simulations

Highly resolved direct numerical simulation (DNS) of decaying homogeneous isotropic turbulence has been carried out. The DNS solves the incompressible Navier-Stokes equations by a pseudo-spectral method in a triply periodic cubic box with size 2π . Similar to the approach by Mansour and Wray [27], the Navier-Stokes equations are formulated in spectral space as

$$\frac{\partial}{\partial t} \left(\hat{u}_i \exp(\nu\kappa^2 t) \right) = \exp(\nu\kappa^2 t) P_{ij} \hat{H}_j, \quad (3)$$

where

$$\hat{H}_j = -i\kappa_i \mathcal{F} (u_i u_j) \quad (4)$$

is the Fourier transform of the non-linear term and $P_{ij} = \delta_{ij} - \kappa_i \kappa_j / \kappa^2$ is the projection operator that imposes incompressibility. Einstein's summation convention is used, which implies summation over indices appearing twice. In eq. (3), the wave-number vector is denoted by $\boldsymbol{\kappa}$, the Fourier transform of the

velocity field is denoted by $\hat{\mathbf{u}}$, and ν is the kinematic viscosity. An integrating factor technique is used for an exact integration of the viscous term. Temporal integration is carried out by a low-storage, stability preserving, third-order Runge-Kutta scheme. The non-linear term is computed in physical space and a truncation technique with a smooth spectral filter is applied to reduce aliasing errors, see Hou and Li [22]. The library P3DFFT has been used for spatial decomposition and to perform the fast Fourier transform [31]. The code employs a hybrid MPI/OpenMP parallelization. The simulations used more than 1.8 Million concurrent threads and have been carried out on the super-computer JUQUEEN at research center Juelich [46]. More details about the numerical procedure and the parallelization strategy are given by Gauding et al. [14, 16] and Goebbert et al. [18, 19].

A necessary constraint that has to be satisfied by the DNS is an adequate resolution of all relevant scales. For the specific case of decaying turbulence this requires resolving the smallest scales down to the viscous cut-off scale, while keeping the integral length-scale l_t , defined as

$$l_t = \frac{3\pi}{4} \frac{\int \kappa^{-1} E(\kappa) d\kappa}{\int E(\kappa) d\kappa}, \quad (5)$$

small compared to the size of the computational domain to reduce confinement effects. Following Mansour and Wray [27], we require that the resolution condition $\kappa_{\max} \eta \geq 1$ is satisfied for all times, where η is the Kolmogorov length-scale and κ_{\max} is the largest resolved wave-number. A grid resolution of 4096^3 points is used to appropriately account for all relevant length-scales.

The initial velocity field is generated in spectral space to be random and statistically isotropic. It satisfies incompressibility and obeys a prescribed energy spectrum of the Batchelor-Proudman type [4], i.e.

$$E(\kappa, 0) \propto \kappa^4 \exp\left(-2\left(\frac{\kappa}{\kappa_p}\right)^2\right). \quad (6)$$

In eq. (6), $\kappa_p = 15$ is the wave-number at which the maximum of the initial spectrum $E(\kappa, 0)$ occurs. The chosen value of κ_p is a compromise between limiting the confinement effect imposed through the finite size of the computational domain and the goal of reaching a high Reynolds number. Following Ishida et al. [23], the initial state of freely decaying turbulence may be described by a Reynolds number defined as

$$Re_0 = \frac{u'_0}{\kappa_p \nu}. \quad (7)$$

Table 1: Initial properties of the DNS.

| | |
|--------------------------------------|----------------------|
| Grid size N^3 | 4096 ³ |
| Peak wave-number κ_p | 15 |
| Viscosity ν | $1.82 \cdot 10^{-4}$ |
| Reynolds number $u'_0/(\nu\kappa_p)$ | 945 |
| Turbulence intensity u'_0 | 2.58 |
| Schmidt number Sc | 1 |
| Integral length-scale l_t | 0.2 |

With a kinematic viscosity of $\nu = 1.82 \cdot 10^{-4}$, and an initial turbulence intensity $u'_0 = 2.58$, where $u'^2 = \frac{2}{3}\langle k \rangle = \frac{1}{3}\langle u_i^2 \rangle$, we obtain an initial Reynolds number Re_0 of 945. Further details of the initialization of the simulation are presented in table 1.

Prescribing a κ^4 energy spectrum at the small wave-numbers is equivalent to a conservation of Loitsyansky's integral [11, 38] and requires

$$\langle k \rangle l_t^5 = \text{constant}. \quad (8)$$

Equation (8) implies a temporal decay of the mean turbulent energy and the mean dissipation as $\langle k \rangle \propto t^{-10/7}$ and $\langle \varepsilon \rangle \propto t^{-17/7}$, respectively. The DNS recovers these scaling laws after an initial transient for $t > 0.3$ over nearly two decades, cf. fig. 2. In the following, we refer to this range as the self-similar decay. However, it is important to note that Batchelor-Proudman turbulence with $E(\kappa) \propto \kappa^4$ is not completely self-similar. Complete self-similarity requires a constant Reynolds number, which is possible in decaying homogeneous isotropic turbulence only under the condition that the turbulent kinetic energy and the energy dissipation decay as $\langle k \rangle \propto t^{-1}$, and $\langle \varepsilon \rangle \propto t^{-2}$, respectively, see Ristorcelli [36, 37] and references therein.

For the analysis of turbulent mixing, an additional advection-diffusion equation for the scalar fluctuations $\phi(\mathbf{x}, t)$ is solved, i.e.

$$\frac{\partial \phi}{\partial t} + u_i \frac{\partial \phi}{\partial x_i} = D \frac{\partial^2 \phi}{\partial x_i^2} - \Gamma u_2, \quad (9)$$

where D is the molecular diffusivity. In the following, we consider a unity Schmidt number meaning that the kinematic viscosity ν equals the molecular diffusivity D . A uniform mean scalar gradient Γ is imposed on the scalar field. In this configuration, the velocity field is decaying while the scalar field is subject to a continuous injection of energy at the large scales. A similar flow configuration was studied experimentally by Bahri et al. [3] and Warhaft

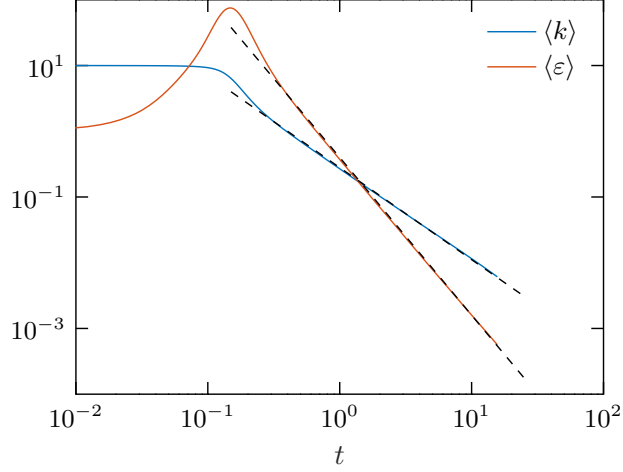


Figure 2: Temporal evolution of $\langle k \rangle$ and $\langle \varepsilon \rangle$ obtained from DNS. The black dashed lines refer to the analytical scaling exponents of $-10/7$ and $-17/7$, respectively.

[58]. The scalar field is initialized with delta-correlated fluctuations at low intensity that are initially uncorrelated with the velocity field, i.e. $\langle u_i \phi \rangle = 0$. By this approach, scalar structures develop naturally from the non-linear coupling to the velocity field and the injection of energy by the mean scalar gradient Γ .

The scalar variance $\langle \phi^2 \rangle$ is governed by the evolution equation

$$\frac{\partial \langle \phi^2 \rangle}{\partial t} = -2\Gamma \langle u_2 \phi \rangle - \langle \chi \rangle, \quad (10)$$

where $\langle \chi \rangle$ is the mean scalar dissipation, defined as

$$\langle \chi \rangle = 2D \left\langle \left(\frac{\partial \phi}{\partial x_i} \right)^2 \right\rangle. \quad (11)$$

Equation (10) shows that the change of the scalar variance is determined by a balance between production $-2\Gamma \langle u_2 \phi \rangle$ and dissipation $\langle \chi \rangle$ of scalar energy, see fig. 3 for a temporal evolution of these terms. After the initial transient, production of scalar energy exceeds scalar dissipation resulting in a temporal increases of $\langle \phi^2 \rangle$. We note in passing that all terms in eq. (10) reveal after the initial transient a power-law scaling.

To further characterize the DNS, it is meaningful to analyze the transport equation for the mean scalar dissipation, which can be written as

$$\frac{1}{\langle \chi \rangle} \frac{d\langle \chi \rangle}{dt} = -4 \sqrt{\frac{\langle \varepsilon \rangle}{\nu}} \left((S_\phi + S_\Gamma) + \sqrt{\frac{5}{3}} \frac{G_\phi}{Re_\lambda R} \right). \quad (12)$$

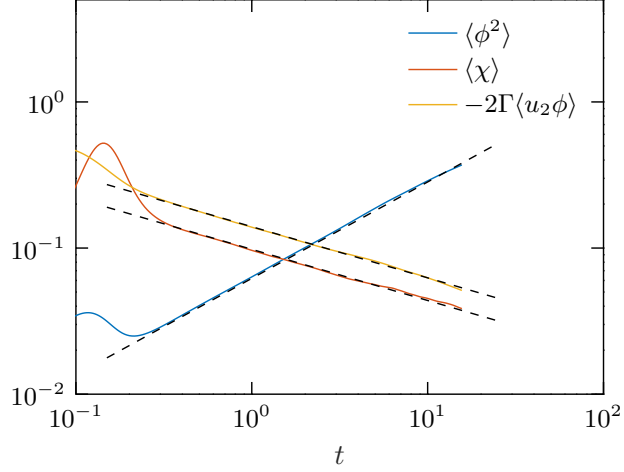


Figure 3: Temporal evolution of the scalar variance $\langle \phi^2 \rangle$ and its production $-2\Gamma \langle u_2 \phi \rangle$ and dissipation $\langle \chi \rangle$. The black dashed lines are displayed as a visual guide to indicate power-law scaling.

Equation (12) generalizes the derivation by Gonzalez and Fall [20], Zhou et al. [60], and Danaila and Mydlarski [9] to statistically homogeneous but anisotropic turbulence with large-scale production. In eq. (12), we introduced the mixed velocity-scalar gradient skewness

$$S_\phi = \frac{\langle g_i g_j A_{ij} \rangle}{\langle g^2 \rangle \langle A_{kl}^2 \rangle^{1/2}}, \quad (13)$$

the scalar gradient destruction coefficient

$$G_\phi = \frac{\langle \phi^2 \rangle}{\langle g^2 \rangle^2} \left\langle \left(\frac{\partial^2 \phi}{\partial x_i \partial x_k} \right)^2 \right\rangle, \quad (14)$$

and the normalized scalar gradient production due to the mean gradient Γ

$$S_\Gamma = \frac{\Gamma \langle g_k A_{2k} \rangle}{\langle g^2 \rangle \langle A_{ij}^2 \rangle^{1/2}}. \quad (15)$$

The velocity gradient tensor is given by $A_{ij} = \partial u_i / \partial x_j$, the scalar gradient is denoted by $g_i = \partial \phi / \partial x_i$, and the velocity-scalar time-scale ratio is defined as

$$R = \frac{\langle \phi^2 \rangle}{\langle \chi \rangle} \frac{\langle \varepsilon \rangle}{\langle u_i^2 \rangle}. \quad (16)$$

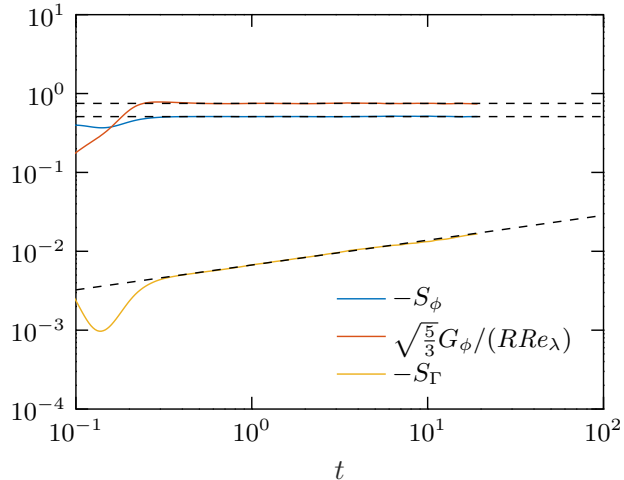


Figure 4: Temporal evolution of the normalized production of scalar dissipation by vortex stretching $-S_\phi$ and mean scalar gradient $-S_\Gamma$, and normalized destruction of scalar dissipation by diffusion $\sqrt{\frac{5}{3}}G_\phi/(RRe_\lambda)$. The black dashed lines are displayed as a visual guide.

During the self-similar decay, the velocity-scalar time-scale ratio R is virtually constant and equals approximately 1.1 for the present DNS. Equation (12) contains two different production mechanisms for the mean scalar dissipation: small-scale production due to the vortex-stretching mechanism of turbulence [6] described by $-S_\phi$, and large-scale production due to the mean scalar gradient Γ covered by the term $-S_\Gamma$. Destruction of scalar dissipation results from molecular diffusivity and is described by G_ϕ . Figure 4 displays the temporal evolution of the different terms. Both terms, $-S_\phi$ and $\sqrt{5/3}G_\phi/(RRe_\lambda)$, tend to a constant, where the destruction $\sqrt{5/3}G_\phi/(RRe_\lambda)$ prevails over the production $-S_\phi$. The production of scalar dissipation by the mean scalar gradient $-S_\Gamma$ increases by following a power-law with time, but remains negligible compared to production by vortex stretching $-S_\phi$. The contribution of the large-scale production $-S_\Gamma$ to the budget in eq. (12) gains importance during the self-similar decay. This results from a decrease of the Reynolds number, which leads to a reduced scale separation between small and large scales.

Under the influence of a mean scalar gradient, statistics of the scalar field are characterized by an anisotropy, such as a non-zero scalar gradient

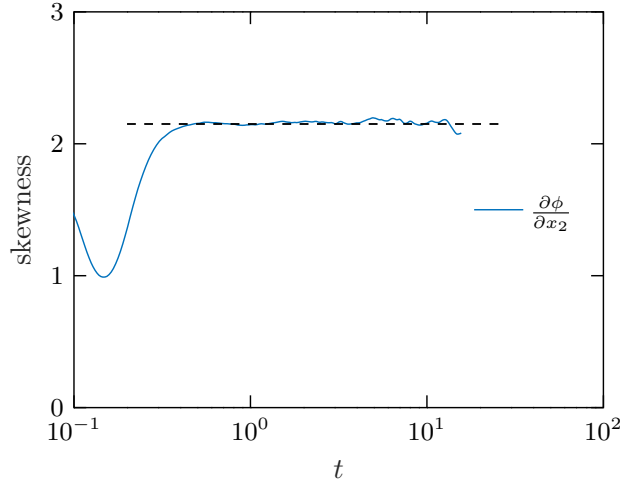


Figure 5: Temporal evolution of the scalar gradient skewness S in x_2 -direction (parallel to the direction of the scalar mean gradient). The black dashed line refers to a constant value of 2.16. The scalar gradient skewness perpendicular to the scalar mean gradient (not shown) is zero.

skewness, i.e.

$$S = \frac{\langle \left(\frac{\partial \phi}{\partial x_2} \right)^3 \rangle}{\langle \left(\frac{\partial \phi}{\partial x_2} \right)^2 \rangle^{3/2}}, \quad (17)$$

in the direction of the mean scalar gradient [5, 44, 49]. The non-zero skewness originates from a preferential alignment of coherent scalar structures with the direction of the mean scalar gradient, which manifest themselves as cliffs and ramps, i.e. steep gradients followed by relatively well mixed regions [6]. Figure 5 shows the temporal evolution of the scalar gradient skewness S . During the self-similar decay, S approaches a nearly constant value close to 2.16. The scalar signal in planes perpendicular to the scalar mean gradient does not exhibit a statistical asymmetry, and the scalar gradient skewness in these directions is zero.

Characteristic properties of the DNS are summarized in table 2 for six different time steps (denoted by D1-D6) that are used for further analysis. During that time, the Taylor-based Reynolds number decreases by nearly a factor of 2 from 95.8 to 54.6. Ensemble-averages (denoted by angular brackets) are computed by virtue of homogeneity over all grid points in the computational domain, and additionally, to improve accuracy of statistical quantities, over three statistically independent realizations of the DNS. With

Table 2: Characteristic properties of the DNS at different t

| | D1 | D2 | D3 | D4 | D5 | D6 |
|-----------------------------------|--------|--------|--------|--------|--------|--------|
| t | 0.5 | 0.9 | 2 | 4 | 7 | 10.3 |
| $\langle k \rangle$ | 0.7468 | 0.3097 | 0.1034 | 0.0402 | 0.0187 | 0.0109 |
| $\langle \varepsilon \rangle$ | 2.2243 | 0.4768 | 0.0705 | 0.0137 | 0.0037 | 0.0015 |
| Re_λ | 95.8 | 85.8 | 74.5 | 65.7 | 59.1 | 54.6 |
| l_t | 0.38 | 0.47 | 0.63 | 0.79 | 0.95 | 1.05 |
| $\langle \phi^2 \rangle$ | 0.0388 | 0.0587 | 0.0993 | 0.1590 | 0.2330 | 0.3036 |
| $\langle \chi \rangle$ | 0.1246 | 0.0998 | 0.0753 | 0.0593 | 0.0500 | 0.0443 |
| $-2\Gamma\langle u_2\phi \rangle$ | 0.0897 | 0.0714 | 0.0541 | 0.0435 | 0.0363 | 0.0317 |
| R | 1.07 | 1.10 | 1.11 | 1.09 | 1.09 | 1.09 |
| S | 2.15 | 2.15 | 2.17 | 2.17 | 2.16 | 2.15 |
| $\kappa_{\max}\eta$ | 2.15 | 3.16 | 5.10 | 7.69 | 10.69 | 13.45 |

this procedure, at each time step, statistics are computed over more than 200 Billion grid points. Figure 6 displays a visualization of the scalar iso-surface for two different time steps. At the early time step (D2), the scalar iso-surface is strongly twisted and folded and reveals regions of high curvature. During the self-similar decay, the iso-surface is smoothed and larger coherent structures are visible.

Finding the local extremal points of the signal ϕ along a straight line in direction x_1 turns into the problem of finding the roots of its first derivative $\phi_x = \partial\phi/\partial x_1$. The derivatives of ϕ are calculated by a spectral method and exactly interpolated to a finer mesh. On this new mesh, the zero-crossings of the first derivative act as the starting points for a Newton iteration that yields the exact position of the extremal points. Detecting local extremal points to define line segments requires a sufficiently smooth and well resolved turbulent field. In order to appropriately identify line segments, we require that the turbulent scalar field can be locally expanded as a Taylor series up to order two. This is equivalent to the condition that the turbulent scalar field is locally two times continuously differentiable. If this condition is violated, statistics of line segments are under-resolved. From parameter studies, we found $\kappa_{\max}\eta \geq 2.5$ to be a necessary condition. Therefore, we report results for line segments for $t \geq 0.9$.

In the following, we present the analysis of the DNS by line segments with a special emphasis on the question whether statistics of line segments are self-similar. Line segments are computed in x_1 -direction, which is perpendicular to the mean scalar gradient. The effect of anisotropy is discussed

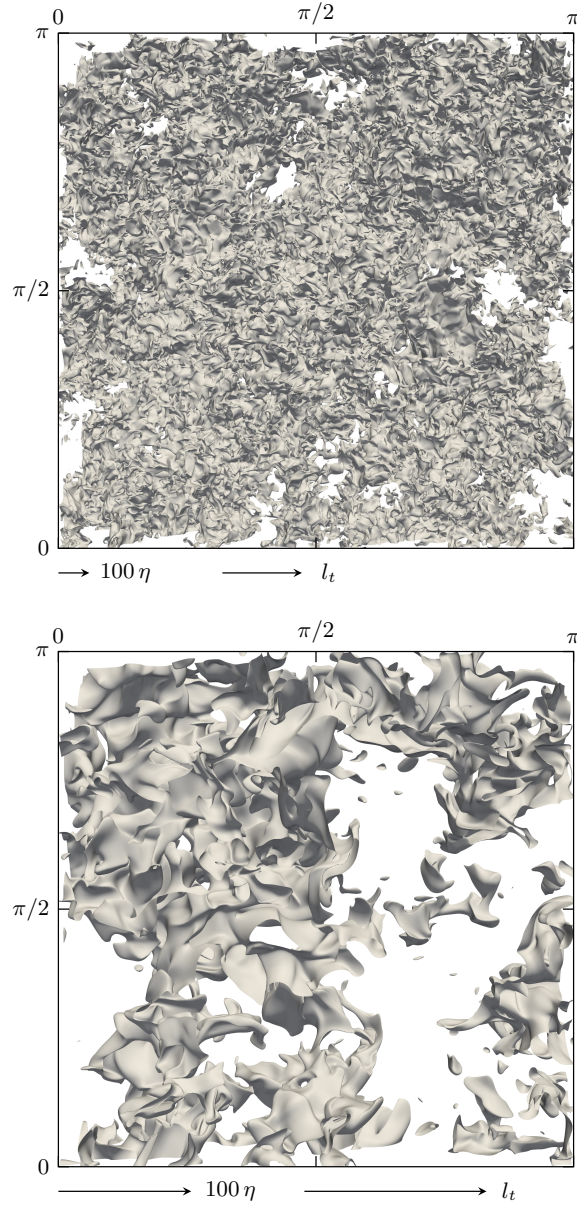


Figure 6: Visualization of the iso-scalar surface obtained from case D2 (top) and case D6. Only a subset of the computational domain of size $\pi \times \pi \times \pi/4$ is shown for clarity. The length of the arrows represents 100 times the Kolmogorov length scale η and the integral length scale l_t , respectively.

in Appendix A.

3. The length distribution of line segments

Two characteristic parameters, the length ℓ and the scalar difference $\Delta\phi$ have been defined to characterize line segments. The linear length ℓ between adjacent extremal points provides a measure for the length-scales present in turbulent fields. Figure 7 (top) shows the length-distribution $P(\ell)$ for different time steps during the decay. It is observed that the curves do not collapse and that for later times, the maximum of $P(\ell)$ is shifted towards larger scales. In other words: the mean length ℓ_m of dissipation elements, which is related to $P(\ell)$ by

$$\ell_m = \int_0^\infty \ell P(\ell) d\ell, \quad (18)$$

increases during the decay. This finding is in agreement with the increase of all other turbulent length-scales in decaying turbulence.

Figure 7 (bottom) shows the probability density function (pdf) of ℓ , rescaled with the respective mean length ℓ_m for each time step. By normalization with a single parameter, namely, the mean length ℓ_m , the pdfs of the length collapse to a single curve. This finding indicates that the pdf of the non-dimensional length $\tilde{\ell} = \ell/\ell_m$, which can be calculated as

$$\tilde{P}(\tilde{\ell}) = \ell_m P(\ell/\ell_m) \quad (19)$$

is completely self-similar in decaying turbulence. It is worth mentioning that self-similarity of $\tilde{P}(\tilde{\ell})$ was observed before in homogeneous isotropic forced turbulence for a broad range of the Reynolds numbers between $Re_\lambda = 88$ and $Re_\lambda = 529$, cf. Gauding et al. [16]. By definition, $\tilde{P}(\tilde{\ell})$ satisfies two constraints, i.e.

$$\int_0^\infty \tilde{P}(\tilde{\ell}) d\tilde{\ell} = 1, \quad (20)$$

and

$$\int_0^\infty \tilde{\ell} \tilde{P}(\tilde{\ell}) d\tilde{\ell} = 1. \quad (21)$$

As displayed in fig. 7, $\tilde{P}(\tilde{\ell})$ declines steeply towards the origin as small segments are annihilated by molecular diffusion. For larger length-scales the pdf exhibits a clear exponential decay indicating that these segments are governed by a Poisson process (see inset of fig. 7). This is plausible as for larger length-scales the probability of the occurrence of an extremal point is

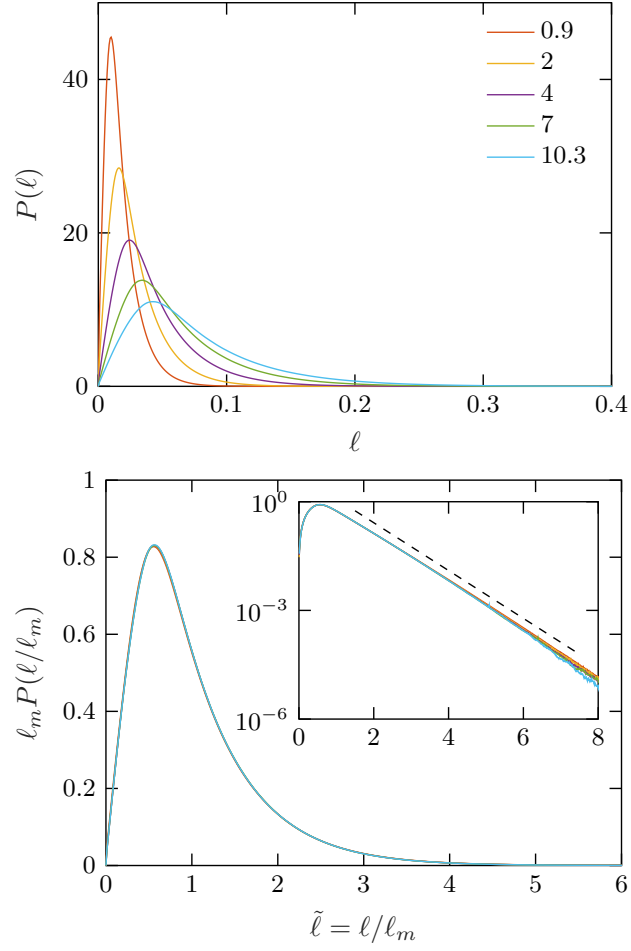


Figure 7: Length distribution $P(\ell)$ of line segments (top), and normalized length distribution $\tilde{P}(\tilde{\ell}) = \ell_m P(\ell/\ell_m)$ (bottom) for different time steps. The black dashed line in the inset indicates an exponential tail, i.e. $\tilde{P}(\tilde{\ell}) \propto \exp(-1.5\tilde{\ell})$.

independent of the adjacent ones. The non-gaussianity of $\tilde{P}(\tilde{\ell})$ is a feature that is shared with the pdf of other turbulent quantities, such as the pdf of the scalar gradient or scalar increment [21, 34, 58]. However, different from these quantities, $\tilde{P}(\tilde{\ell})$ reveals complete self-similarity under rescaling with a single length-scale. The pdfs of scalar gradients or increments cannot be superposed by a non-trivial rescaling procedure, because of the existence of stretched exponential tails, which depend on either Reynolds number, length-scale or other non-universal features. For comparison, further statistics of the scalar gradient will be presented in sec. 4.

DNS suggests that the mean length ℓ_m is the only characteristic length-scale for the normalized distribution function $\tilde{P}(\tilde{\ell})$. To obtain the dimensional pdf $P(\ell)$ from the normalized pdf $\tilde{P}(\tilde{\ell})$, the scaling of the normalization quantity, i.e. the mean length ℓ_m , is required. This information is provided by fig. 8, where the normalized mean length ℓ_m/η is shown as the function of the Taylor-based Reynolds number. The DNS results indicate that the mean length ℓ_m scales with the Kolmogorov length-scale, i.e.

$$\ell_m \approx 10\eta. \quad (22)$$

Equation (22) is well satisfied for scalar fields in decaying turbulence and forced turbulence [16] for a wide range of different Reynolds numbers. However, the proportionality constant given in eq. (22) may not be universal and may depend on the large-scales of the flow. Moreover, the proportionality constant is flow-field dependent and is, for example, different for the signal of the longitudinal or transversal velocity components. In the next paragraph, we provide a justification for the scaling relation given by eq. (22) based on a statistical theory developed by Rice [35].

Rice [35] proved that for any homogeneous Gaussian stochastic process $\phi(x)$, the number of zero-crossings is given by

$$N_0 = \frac{1}{\pi} \left[-\frac{f_\phi''(0)}{f_\phi(0)} \right]^{1/2}. \quad (23)$$

In eq. (23), f_ϕ is the normalized correlation function of the signal $\phi(x)$, defined as

$$f_\phi(r) = \frac{\langle \phi(x)\phi(x+r) \rangle}{\langle \phi^2 \rangle}, \quad (24)$$

and $f_\phi''(r)$ is the second derivative of $f_\phi(r)$. By virtue of homogeneity, the correlation functions depend only on the separation distance r . Liepmann [26] and Sreenivasan et al. [43] found from experiments that eq. (23) is

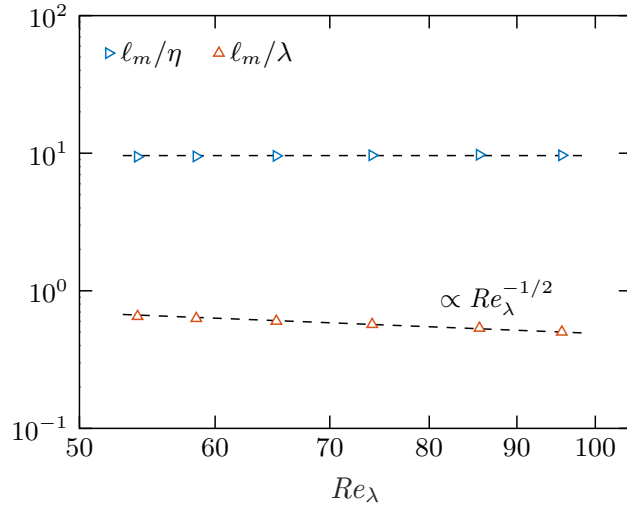


Figure 8: Scaling of the mean length ℓ_m of line segments with the Kolmogorov length-scale η and the Taylor micro-scale λ as a function of Re_λ .

valid for the turbulent velocity field, despite the fact that turbulence is clearly not Gaussian. Liepmann [26] noticed that for the validity of eq. (23), essential statistical independence between $\phi(x)$ and its first derivative $\phi_x(x)$ is required.

This observation encouraged Schaefer et al. [39] and Gauding et al. [16] to adopt Rice's theorem to estimate the number of extremal points N_E of a turbulent signal $\phi(x)$ as

$$N_E \propto \left[-\frac{f''_{\phi_x}(0)}{f_{\phi_x}(0)} \right]^{1/2}, \quad (25)$$

where f_{ϕ_x} is the normalized derivative correlation function defined as

$$f_{\phi_x}(r) = \frac{\langle \phi_x(x)\phi_x(x+r) \rangle}{\langle \phi_x^2 \rangle}. \quad (26)$$

Equation (25) makes use of the fact that the extremal points of $\phi(x)$ turn into zero-crossings of the derivative signal $\phi_x(x)$. With eq. (25) at hand, we can deduce the scaling of the mean length ℓ_m solely from properties of the derivative correlation function f_{ϕ_x} .

In fig. 9, we display the normalized correlation function f_ϕ and the normalized derivative correlation function f_{ϕ_x} for different time steps during

the self-similar decay as a function of r/η . Significant differences between $f_\phi(r/\eta)$ and $f_{\phi_x}(r/\eta)$ are evident, i.e. the correlation length for the scalar is much larger than that of the scalar gradient. The derivative correlation function $f_{\phi_x}(r/\eta)$ decays fast and becomes negative with a zero-crossing at $r/\eta \approx 1.6$ and a minimum at $r/\eta \approx 3.2$. This behavior can be explained from the general property that correlation functions of derivatives have zero integral length-scale l_{ϕ_x} , i.e.

$$l_{\phi_x} = \int_0^\infty f_{\phi_x}(r)dr = - \int_0^\infty \frac{d^2}{dr^2} f_\phi(r)dr = 0, \quad (27)$$

where the second equality follows from homogeneity of $\phi_x(x)$, and the third equality requires $f_\phi(r)$ to decay to zero for $r \rightarrow \infty$. A necessary condition following from eq. (27) for $f_{\phi_x}(r/\eta)$ is the mutual cancellation between the areas below and above the abscissa. With these constraints, an almost perfect collapse of the normalized derivative correlation functions f_{ϕ_x} for the different time steps can be observed when plotted as a function of r/η , cf. fig. 9. The quality of the collapse is remarkable considering that during the reported period, the scalar gradient variance $\langle \phi_x^2 \rangle$ and the Taylor-based Reynolds number Re_λ decrease by a factor of 2.8 and 1.8, respectively. The collapse of the normalized derivative correlation functions indicates complete self-similarity of $f_{\phi_x}(r/\eta)$. When $f_{\phi_x}(r/\eta)$ becomes self-similar by rescaling with a single length-scale η , eq. (25) requires with $\ell_m \propto 1/N_E$ a scaling of the mean length ℓ_m with the Kolmogorov length-scale η .

Further justification for Kolmogorov scaling of the mean length ℓ_m can be provided by expressing the correlation functions in eq. (25) by one-point quantities, i.e. $f_{\phi_x}(0) = \langle \phi_x^2 \rangle$ and $f''_{\phi_x}(0) = -\langle \phi_{xx}^2 \rangle$, and assuming KOC scaling for these quantities,

$$\langle \phi_x^2 \rangle^{1/2} \propto D^{-1/2} \langle \chi \rangle^{1/2} \quad (28)$$

and

$$\langle \phi_{xx}^2 \rangle^{1/2} \propto \nu^{-1/4} D^{-1} \langle \chi \rangle^{1/2} \langle \varepsilon \rangle^{1/4}. \quad (29)$$

Using (28) and (29) in eq. (25), confirms, with $N_E = 1/\ell_m$, Kolmogorov scaling for the mean length ℓ_m , i.e.

$$\ell_m \propto \eta \propto \lambda Re_\lambda^{-1/2}, \quad (30)$$

where we considered in (30) a unity Schmidt number.

The temporal evolution of line segments in decaying turbulence is governed by a complex process, involving slow and fast changes as discussed by Wang

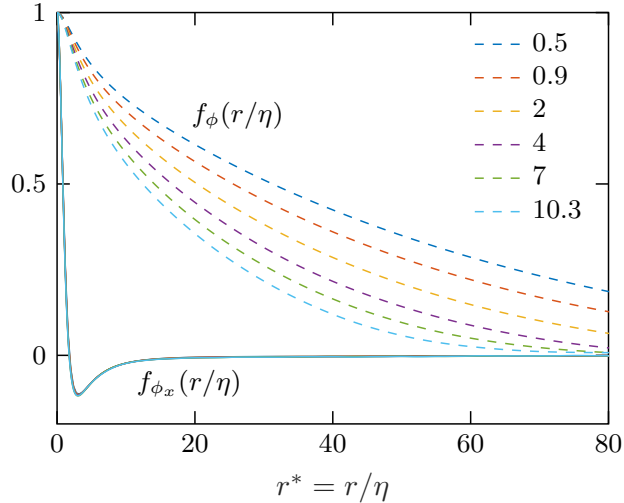


Figure 9: Normalized two-point correlation function of the scalar $f_\phi(r/\eta) = \langle \phi(x+r)\phi(x) \rangle / \langle \phi^2 \rangle$ (dashed lines) and the scalar derivative $f_{\phi_x}(r/\eta) = \langle \phi_x(x+r)\phi_x(x) \rangle / \langle \phi_x^2 \rangle$, displayed for the time steps indicated in table 2. The normalized scalar derivative two-point correlation function becomes self-similar when plotted as a function of $r^* = r/\eta$.

and Peters [55] and Schaefer et al. [40]. Slow changes are responsible for a continuous evolution of the ending points. As the ending points are moved relatively to each other, slow changes can modify the length distribution function $P(\ell)$ but not the mean length ℓ_m . On the other hand, fast changes describe processes where the connectivity of line segments changes abruptly due to a topology change of the scalar field. An abrupt topology change occurs when local extremal points disappear due to diffusion or when new local extremal points appear due to the stretching and folding mechanism of turbulent flows. This process results in a discrete change of both $\Delta\phi$ and ℓ , and can hence modify the mean length ℓ_m . Wang and Peters [55] distinguished between two different fast processes. By a reconnection process, two initially independent dissipation elements are merged and a new dissipation element with a larger $\Delta\phi$ is created. A splitting process, on the other hand, generates new local extremal points resulting in a shortening of line segments and in an abrupt decrease of $\Delta\phi$. Figure 10 illustrates a cutting and reconnection process. Following Wang [51], the mean length of line segments is governed by the evolution equation

$$\frac{1}{\ell_m} \frac{d\ell_m}{dt} = \ell_m \Lambda_1 - 2\Lambda_2 \quad (31)$$

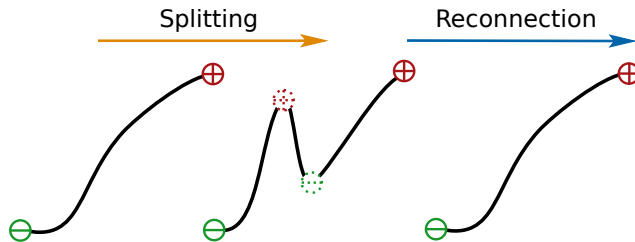


Figure 10: Illustration of a splitting and reconnection event. By splitting, a line segment is divided into three smaller segments by introducing new extremal points. Reconnection refers to an event when extremal points disappear, i.e. due to diffusion, and smaller elements are joint to form one large segment.

where Λ_1 and Λ_2 denote the frequencies of generation and annihilation of extremal points, respectively. Physically, Λ_1 is determined by the turbulence intensity, while Λ_2 is determined by the molecular diffusivity and the mean length-scale. In decaying turbulence, the turbulence intensity decreases and molecular diffusion smooths the scalar field. As a consequence, the annihilation process prevails over the generation process leading to the observed increase of the mean length ℓ_m , or, the decrease of the number of extremal points N_E .

4. The joint distribution of $\Delta\phi$ and ℓ

Turbulent flows are characterized by a complex spatio-temporal structure with a non-local interaction between various length-scales. Conventionally, more understanding of the spatial flow structure can be obtained from two-point or multi-point statistics, rather than one-point statistics. Line segments are parameterized by the distance ℓ and the scalar difference $\Delta\phi$ between adjacent extremal points. Then, most statistical properties are captured by the joint statistics of these parameters. The Bayes theorem relates the marginal pdf $P(\ell)$ of the length of line segments to the joint and conditional pdfs by

$$P_c(\Delta\phi|\ell) = \frac{P(\Delta\phi, \ell)}{P(\ell)}, \quad (32)$$

where $P_c(\Delta\phi|\ell)$ refers to the conditional pdf, and $P(\Delta\phi, \ell)$ is the joint probability density function (jpdf).

Figure 11 shows the normalized joint probability density function $P(\Delta\phi, \ell)$ for two different time steps D1 and D6 during the self-similar decay. The abscissa is normalized by the Kolmogorov length η and the ordinate is normalized by the standard deviation $\sigma_{\Delta\phi}$, given by $\sigma_{\Delta\phi} = \langle(\Delta\phi)^2\rangle^{1/2}$. The

jpdf exhibits two distinct wings, where the upper wing corresponds to positive segments with $\Delta\phi > 0$, and the lower wing corresponds to negative segments with $\Delta\phi < 0$. The scale-dependent skewness $\langle(\Delta\phi)^3|\ell\rangle/\langle(\Delta\phi)^2|\ell\rangle^{3/2}$ is close to zero for all scales ℓ , which signifies that the wings are symmetric with respect to the abscissa. Figure 11 also displays the conditional normalized mean scalar difference $\langle\Delta\phi|\ell/\eta\rangle/\sigma_{\Delta\phi}$ separately for positive and negative segments. The magnitude of the conditional mean increases monotonously with ℓ/η . It can be concluded that $\Delta\phi$ and ℓ are not independent and that on average, large segments also have a large scalar difference. The jpdf $P(\Delta\phi, \ell)$ covers different physical effects. The upper and lower left corners, where ℓ is small but the magnitude of $\Delta\phi$ is large, represent poorly mixed regions, characterized by large absolute values of the mean gradients $g = \Delta\phi/\ell$. Well mixed regions exist close to the abscissa, where the magnitude of $\Delta\phi$ is small and ℓ stays sufficiently large. Comparing the normalized jpdfs for time steps D2 and D5 reveals that the shape of the jpdfs is very similar but not completely self-similar. At the late time step, segments with very large length-scale ℓ/η and segments with very large scalar difference $|\Delta\phi|/\sigma_{\Delta\phi}$ are slightly less significant. This can be explained by the decrease of the Reynolds number and the associated smoothing of the turbulent field. The consequence of this observation on the self-similarity of line segments will be explored in more detail in the next section.

To study turbulent mixing, a line segment based mean gradient can be defined as

$$g = \frac{\Delta\phi}{\ell}, \quad (33)$$

which is proportional to the mean diffusive flux or the mean local scalar gradient between adjacent extremal points, i.e.

$$\frac{1}{\ell} \int_{x_1}^{x_1+\ell} \left(D \frac{\partial\phi}{\partial x_1} \right) dx_1 = D \frac{\Delta\phi}{\ell}. \quad (34)$$

Dimensionally, the mean gradient g can be related to the scalar mean dissipation, i.e.

$$\langle g^2 \rangle \propto \frac{\langle \chi \rangle}{D}. \quad (35)$$

With these properties, the jpdf $P(g, \ell)$ provides information about the scale-dependence of turbulent mixing. The normalized jpdf $P(g, \ell)$ is displayed for two different time steps D2 and D6 in fig. 12. The abscissa is normalized by the Kolmogorov length η and the ordinate is normalized by the rms of g , defined as $\sigma_g = \langle g^2 \rangle^{1/2}$. Similar to $P(\Delta\phi, \ell)$, the jpdf $P(g, \ell)$ has two distinct wings for positive and negative gradients. The wings are symmetric

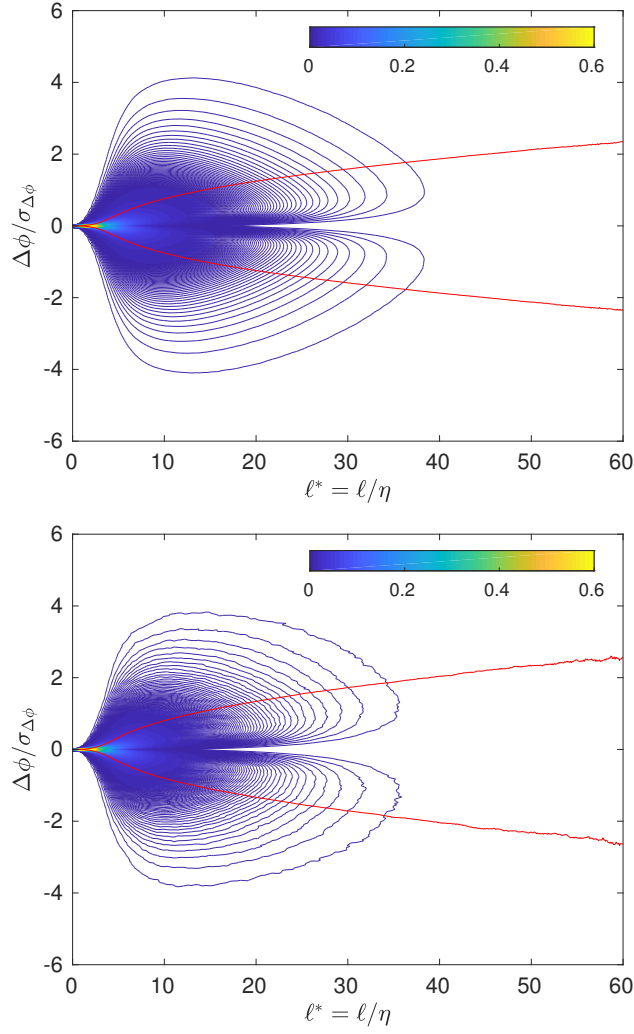


Figure 11: Joint distribution function $P(\Delta\phi, \ell)$ for time step D2 (top) and time step D6. The red lines refer to the normalized conditional average $\langle \Delta\phi | \ell \rangle$, which are shown separately for positive and negative wings.

and reveal with respect to the abscissa a long tail which is situated at small, but finite length-scale ℓ . That means that large gradients occur at a finite length-scale and not in the limit $\ell \rightarrow 0$. This behavior comes from the fact that $\Delta\phi$ and ℓ are not independent. At small scales, $\Delta\phi$ tends rapidly to zero due to molecular damping resulting in vanishing values of g . It is important to emphasize that the scale-dependent scalar gradient based on the scalar increment $\delta\phi$ has a non-zero limit for $r \rightarrow 0$, as the compensated structure function

$$\frac{\langle(\delta\phi)^{2n}\rangle}{r^{2n}} \quad (36)$$

turns into the corresponding moment of local scalar gradient,

$$\lim_{r \rightarrow 0} \frac{\langle(\delta\phi)^{2n}\rangle}{r^{2n}} = \left\langle \left(\frac{\partial\phi}{\partial x_1} \right)^{2n} \right\rangle, \quad (37)$$

in the small-scale limit for $r \rightarrow 0$.

Figure 12 reveals that long line segments are predominantly characterized by small mean gradients g . These line segments represent relatively well mixed regions, which appear as ramp-like structures in the scalar field. For the present DNS, the size of these coherent regions reaches up to 100η .

On the other hand, very large positive and negative values of g can be found at the tips of the wings, which exceed the rms value of g by a factor close to 20 (for case D2) and close to 15 (for case D6). This indicates the existence of strong internal intermittency. In scalar fields, intermittency results from the characteristic cliff-like structure [41], formed by a straining motion, which has its origin in the vortex-stretching mechanism of turbulence. As observed in fig. 12, the normalized jpdf $P(g, \ell)$ is clearly not self-similar, because intermittency weakens during the decay. This result confirms the standard paradigm of turbulence that especially the rare large events break self-similarity.

Intermittency effects are also observed from the pdf of the local scalar gradient $P(\partial\phi/x_1)$, displayed in fig. 13. The normalized pdfs of the scalar gradient are strongly non-gaussian and exhibit stretched exponential tails. The tails of the pdfs, which represent rare extreme events, do not collapse for different time steps: they become less pronounced during the decay and are clearly not self-similar. To quantify the statistical behavior of rare extreme events, the local gradient flatness

$$F = \frac{\left\langle \left(\frac{\partial\phi}{\partial x_1} \right)^4 \right\rangle}{\left\langle \left(\frac{\partial\phi}{\partial x_1} \right)^2 \right\rangle^2}, \quad (38)$$

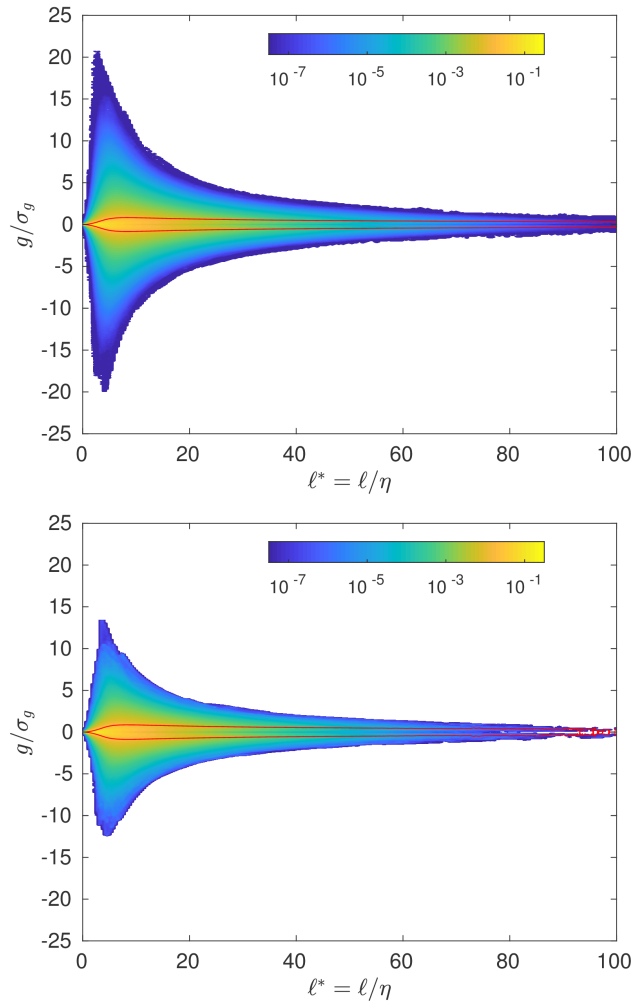


Figure 12: Joint distribution function $P(g, \ell)$ for time step D2 (top) and time step D6. The red lines refer to the normalized conditional average $\langle g|\ell \rangle$, which are shown separately for the positive and negative wings.

and the flatness of the mean gradient of line segments g

$$F_g = \frac{\langle g^4 \rangle}{\langle g^2 \rangle^2}, \quad (39)$$

can be introduced as the normalized fourth-order moment [13]. For line segments, the even order moments of the mean gradient g are given by

$$\langle g^{2n} \rangle = \int_{-\infty}^{\infty} \int_0^{\infty} g^{2n} P(g, \ell) d\ell dg. \quad (40)$$

Figure 14 illustrates the scaling of F and F_g as a function of the Reynolds number Re_λ . From the DNS results, it follows that F and F_g can be approximated by a power-law, i.e. $\propto Re_\lambda^\alpha$ where the scaling exponent α is close to 0.55 for both quantities. Despite virtually the same scaling exponent, F_g is considerably smaller than F , as the segment based gradient g is already an average quantity defined over a stochastic length-scale ℓ . The flatness for both quantities increase with Reynolds number (or alternatively decrease with time). A constant flatness factor is a necessary condition for complete self-similarity, so that we can conclude that in this kind of flow, neither the local gradient $\partial\phi/\partial x_1$ nor the mean gradient of line segments g are self-similar. Note that under the conditions of the KOC theory, which hypothesizes universality of small-scale turbulence, a constant flatness factor is predicted [1, 47].

For reference, fig. 15 shows the Reynolds number dependence of the normalization quantities $\sigma_{\Delta\phi}$ and σ_g . For the investigated range of Reynolds numbers, both quantities scale with good accuracy with the KOC quantities, i.e. $\sigma_{\Delta\phi} \propto \langle \chi \rangle^{1/2} \tau_\eta^{1/2}$ and $\sigma_g \propto \langle \chi \rangle^{1/2} \nu^{-1/2}$, with the Kolmogorov time-scale given by $\tau_\eta = (\nu/\langle \varepsilon \rangle)^{1/2}$.

5. Scaling of the conditional averages $\langle \Delta\phi|\ell \rangle$ and $\langle \Delta u|\ell \rangle$

An n th order conditional average of line segments,

$$\langle |\Delta\phi|^n |\ell \rangle = \int_{-\infty}^{\infty} |\Delta\phi|^n \frac{P(\Delta\phi, \ell)}{P(\ell)} d(\Delta\phi), \quad (41)$$

can be defined. In contrast to the definition of conventional structure functions, i.e.

$$\langle |\delta\phi|^n \rangle = \langle |\phi(x+r) - \phi(x)|^n \rangle, \quad (42)$$

the distance ℓ in (41) is not arbitrarily chosen, but rather determined by the local structure of turbulence, represented by the distance ℓ and the

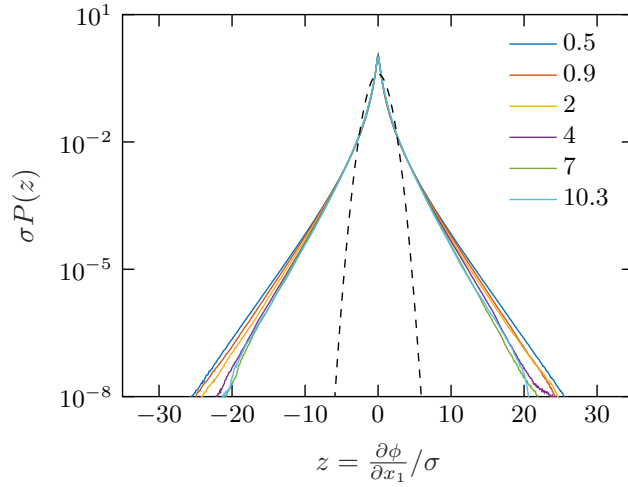


Figure 13: Marginal pdf of the scalar gradient $\partial\phi/\partial x_1$ for different time steps normalized by the standard deviation $\sigma = \langle(\partial\phi/\partial x_1)^2\rangle^{1/2}$ for each curve. The black dashed curve represents a standard normal distribution.

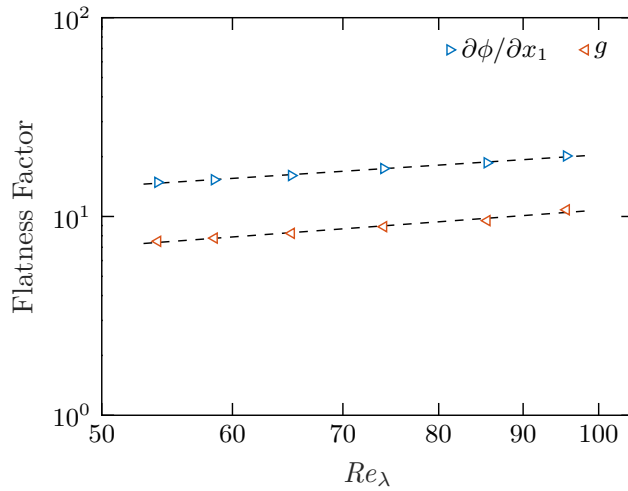


Figure 14: Scaling of the flatness factor of the local scalar gradient $\partial\phi/\partial x_1$ and the segment based mean gradient $g = \Delta\phi/\ell$ as a function of Re_λ . The black dashed lines indicate a least-square fit shown for reference.

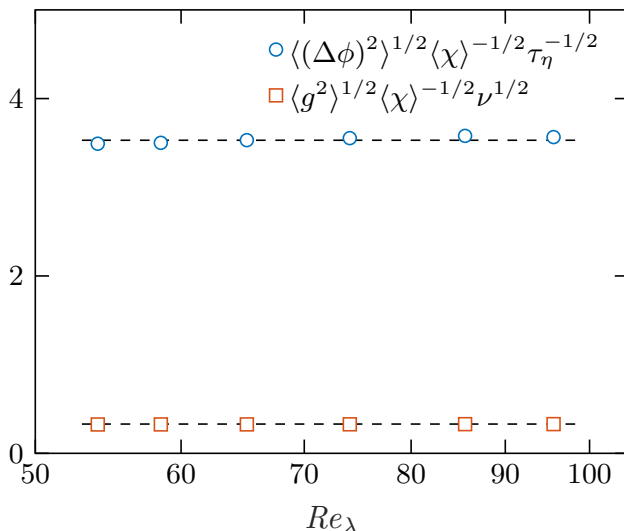


Figure 15: Reynolds number dependence of the normalization quantities $\sigma_{\Delta\phi} = \langle (\Delta\phi)^2 \rangle^{1/2}$ and $\sigma_g = \langle g^2 \rangle^{1/2}$. The dashed lines represent $\sigma_{\Delta\phi} \approx 3.5$ and $\sigma_g \approx 0.3$, respectively.

fluctuations $\Delta\phi$ between adjacent local extremal points. The conditional mean $\langle |\Delta\phi|^n | \ell \rangle$ is computed for segments belonging to the same length-class ℓ , rather than for arbitrary points with the same separation distance r .

Under the assumptions of the KOC theory, statistics of $\Delta\phi$ are uniquely determined by the mean energy dissipation $\langle \varepsilon \rangle$, the mean scalar dissipation $\langle \chi \rangle$ and the molecular diffusivity D . As a straightforward consequence, the conditional average $\langle |\Delta\phi|^n | \ell \rangle$ can be expressed by functional forms,

$$\langle |\Delta\phi|^n | \ell^* \rangle = A_n(t) f_n(\ell^*), \quad (43)$$

that are built as products between a time and order-dependent prefactor $A_n(t)$ and a order-dependent shape function $f_n(\ell^*)$ of the normalized distance ℓ^* . Following the previous findings, we define $\ell^* = \ell/\eta$, with $\eta \propto \ell_m$ being the characteristic length-scale.

Figure 16 shows the normalized conditional mean $\langle |\Delta\phi|^n | \ell \rangle$ for different time steps for $n = 1$ and $n = 5$. Similar to structure functions, the conditional mean exhibits two distinct scaling regimes for small scales in the dissipative range and for larger scales in the inertial range. Normalized with KOC quantities, i.e. $(\langle \chi \rangle \tau_\eta)^{n/2}$, the curves collapse, indicating self-similarity. However, the collapse is much better for the first order $n = 1$ than for the fifth order $n = 5$. This finding is in agreement with the observation that the normalized jpdf of $\Delta\phi$ and ℓ is not completely self-similar for very large

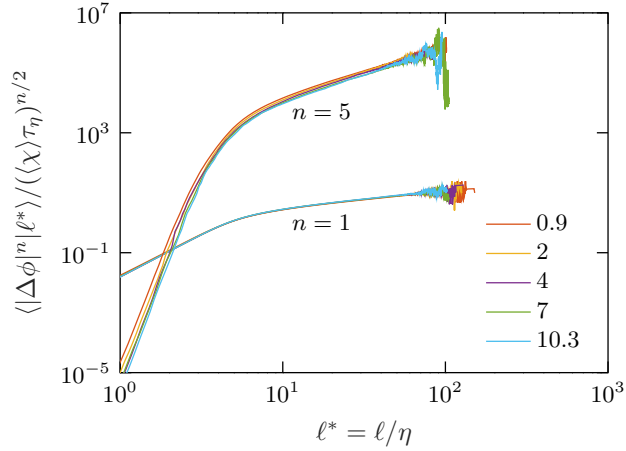


Figure 16: Normalized conditional scalar difference $\langle \Delta\phi^n | \ell \rangle$ for different time steps and for $n = 1$ and $n = 5$.

values of $|\Delta\phi|$ or ℓ . With eq. (41), these parts of the jpdf mostly contribute to higher-order statistics affecting the quality of collapse for the fifth-order structure function. For the first-order conditional average $\langle |\Delta\phi| | \ell \rangle$, primarily the inner parts of $P(\Delta\phi, \ell)$, which are self-similar, contribute to the average.

One of the most important result derived from the incompressible Navier-Stokes equations is the Kolmogorov equation for the velocity structure function [24]. Under the condition of local isotropy and for sufficiently high Reynolds numbers, Kolmogorov hypothesized

$$\langle |\delta u| \rangle \propto (\langle \varepsilon \rangle r)^{1/3}, \quad (44)$$

where δu is the velocity increment taken in longitudinal direction. From a different viewpoint, the velocity difference Δu can be defined with respect to adjacent local extremal points x_{start} and x_{end} of the scalar field [52], i.e.

$$\langle \Delta u | \ell \rangle = \langle u(x_{\text{end}}) - u(x_{\text{start}}) | x_{\text{end}} - x_{\text{start}} = \ell \rangle. \quad (45)$$

The velocity difference Δu is directly connected to a straining motion that is acting on the scalar field. By a straining motion, scalar gradients are smoothed in the direction of extensive strain and steepened in the direction of compressive strain. The balance between strain and diffusion generates the characteristic cliff-ramp-like structure observed in scalar fields. Figure 17 displays the velocity difference $\langle \Delta u | \ell \rangle$ for the different time steps. It can be observed that small segments are subject compressive strain ($\Delta u < 0$),

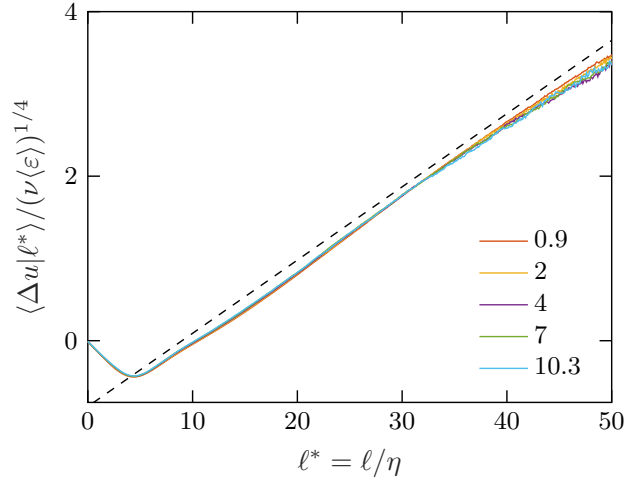


Figure 17: Normalized conditional velocity difference $\langle \Delta u | \ell \rangle$ for different time steps.

while larger segments ($\ell/\eta > 10$) are subject to extensive strain ($\Delta u > 0$). By normalization with the Kolmogorov velocity $u_\eta = (\nu \langle \varepsilon \rangle)^{1/4}$ and the Kolmogorov length-scale η , the curves reveal an excellent collapse for the different time steps indicating complete self-similarity. The increase of $\langle \Delta u | \ell \rangle$ at larger scales, i.e. $\ell/\eta > 10$, is linear, and fig. 17 suggests the scaling relation

$$\langle \Delta u | \ell \rangle \propto \frac{1}{\tau_\eta} \ell. \quad (46)$$

Compared with Kolmogorov's conventional $r^{1/3}$ scaling, cf. (44), a linear scaling with ℓ/τ_η is surprising. It can be explained from the fact that large coherent regions with monotonously varying scalar values are formed preferentially by extensive strain. From dimensional grounds, the straining motion in turbulence scales with the Kolmogorov time τ_η , which leads to eq. (46).

6. Conclusion

The self-similarity of scalar mixing in decaying homogeneous isotropic turbulence has been studied by the method of line segments. By decomposing in one-dimensional space, the method of line segments decomposes the scalar field into smaller sub-units based on local extremal points. Within these sub-units, the value of the scalar varies monotonously. The segments were parameterized by the length ℓ and the scalar difference $\Delta\phi$ between the

ending points. Line segments can be understood as thin local diffusive-convective structures, whose average length ℓ_m equals approximately 10 times the Kolmogorov length scale η . The analysis was based on a highly resolved direct numerical simulation. The main findings are:

1. The length distribution of line segments $P(\ell)$ is strongly non-gaussian. It exhibits a strong dependence on time reflecting the increase of the mean length ℓ_m during the decay. After normalization with the mean length the rescaled pdf $\tilde{P}(\tilde{\ell})$ becomes completely self-similar. A statistical analysis signifies that the mean length ℓ_m scales with the Kolmogorov length-scale η .
2. Further information about the local structure of turbulence is provided by joint statistics of the scalar difference $\Delta\phi$ and the length ℓ . Both quantities are correlated and long segments have on average a large scalar difference $|\Delta\phi|$. The normalized joint pdf reveals a self-similar core, but regions of very large ℓ or very large $|\Delta\phi|$ become slightly less significant during the decay.
3. To investigate turbulent mixing, a line segment based gradient was defined as $g = \Delta\phi/\ell$. Large values of g occur at a small, but finite length-scale. Due to internal intermittency, the joint pdf of g and ℓ exhibits a long tail representing large segment based gradients. These intense gradients stem from cliff-like structures, which are formed by a straining motion. The joint pdf of g and ℓ is clearly not self-similar as gradients with large magnitude disappear during the decay.
4. Consistent with the jpdf $P(\Delta\phi, \ell)$, the normalized conditional average of $\langle \Delta\phi^n | \ell \rangle$ becomes completely self-similar for low orders. Complete self-similarity was not observed for higher-orders, which is in agreement with the standard paradigm of turbulence that higher-order statistics reflect the effect of internal intermittency. The conditional average of the velocity difference, i.e. $\langle \Delta u | \ell \rangle$, allows to assess the impact of a straining motion on the scalar field. In agreement with existing theories, we found that small scales are subject to a compressive strain, while larger length-scales, over which the scalar values varies monotonously, are subject to an extensive strain. It was shown that the normalized conditional velocity difference is self-similar and obeys a linear scaling with the Kolmogorov length and time scales.

Appendix A. Anisotropy of the scalar field

As the scalar field is not isotropic, directional statistics are of interest and provide a deeper insight into cliff-ramp-like structures. Figure A.18 displays

the normalized joint pdfs $P(\Delta\phi, \ell)$ and $P(g, \ell)$ computed for line segments in x_2 -direction (parallel to the mean scalar gradient). The jpdfs display a clear asymmetry with respect to the abscissa, which is different from line segments in x_1 -direction (perpendicular to the mean scalar gradient), cf. figs. 11 and 12. Figure A.18 reveals that increasing line segments ($\Delta\phi > 0$) are on average shorter and have a larger scalar difference compared to decreasing line segments. On the other hand, decreasing line segments ($\Delta\phi < 0$) are on average longer and have a smaller absolute scalar difference. As a consequence, it is more likely that increasing line segments appear as cliff-like structures, while decreasing line segments appear as ramp-like structures. This finding reflects the characteristic cliff-ramp-like structures that exist in the direction parallel to the mean scalar gradient and is in agreement with the positive scalar gradient skewness S displayed in fig. 5.

Acknowledgment

Financial support was provided by the Labex EMC3, under the grant VAVIDEN, as well as the Normandy Region and FEDER. Additionally, the authors gratefully acknowledge the computing time granted on the supercomputer JUQUEEN (Research Center Juelich [46]). The authors would like to thank Dr. Michael Stephan from Juelich Supercomputing Center for his continuous support that helped us to perform simulations with more than 1.8 Million threads.

References

References

- [1] Antonia, R., Tang, S., Djenidi, L., Danaila, L., 2015. Boundedness of the velocity derivative skewness in various turbulent flows. *Journal of Fluid Mechanics* 781, 727–744.
- [2] Antonia, R. A., Smalley, R., Zhou, T., Anselmet, F., Danaila, L., 2003. Similarity of energy structure functions in decaying homogeneous isotropic turbulence. *Journal of Fluid Mechanics* 487, 245–269.
- [3] Bahri, C., Arwatz, G., George, W. K., Mueller, M. E., Hultmark, M., 2015. Self-similarity of passive scalar flow in grid turbulence with a mean cross-stream gradient. *Journal of Fluid Mechanics* 780, 215–225.

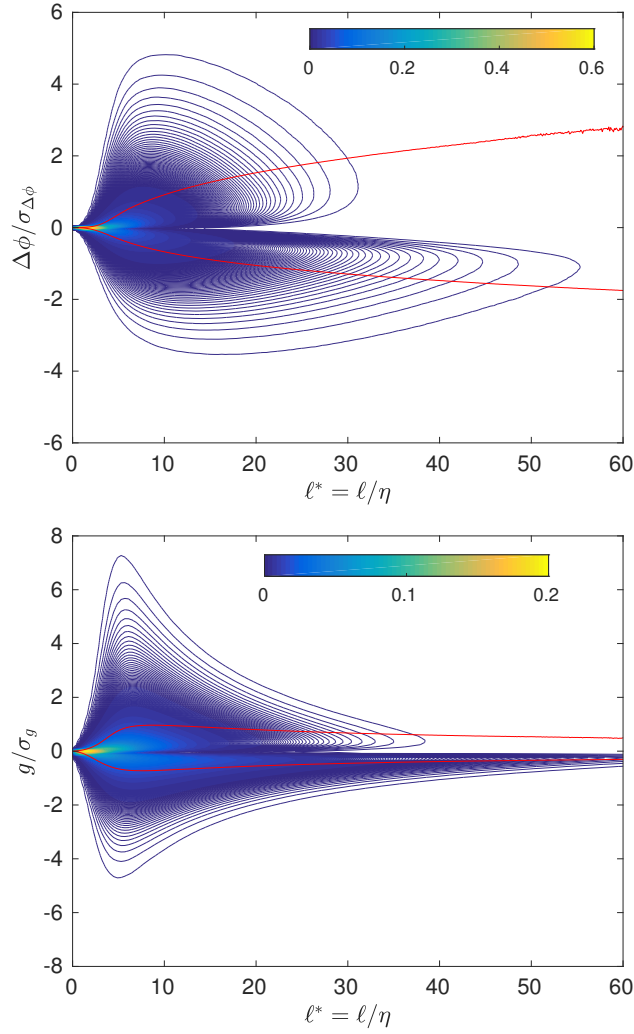


Figure A.18: Joint distribution function $P(\Delta\phi, \ell)$ (top) and joint distribution function $P(g, \ell)$ (bottom) for time step D2. Line segments are computed in x_2 -direction parallel to the mean scalar gradient. The red lines refer to the normalized conditional averages $\langle \Delta\phi | \ell \rangle$ and $\langle g | \ell \rangle$, respectively, which are shown separately for positive and negative wings.

- [4] Batchelor, G. K., Proudman, I., 1956. The large-scale structure of homogenous turbulence. *Phil. Trans. R. Soc. Lond. A* 248 (949), 369–405.
- [5] Bos, W. J., 2014. On the anisotropy of the turbulent passive scalar in the presence of a mean scalar gradient. *Journal of Fluid Mechanics* 744, 38–64.
- [6] Brethouwer, G., Hunt, J., Nieuwstadt, F., 2003. Micro-structure and lagrangian statistics of the scalar field with a mean gradient in isotropic turbulence. *Journal of Fluid Mechanics* 474 (1), 193–225.
- [7] Chakraborty, N., Wang, L., Klein, M., 2014. Streamline segment statistics of premixed flames with nonunity Lewis numbers. *Physical Review E* 89 (3), 033015.
- [8] Corrsin, S., 1951. On the spectrum of isotropic temperature fluctuations in an isotropic turbulence. *Journal of Applied Physics* 22 (4), 469–473.
- [9] Danaila, L., Mydlarski, L., 2001. Effect of gradient production on scalar fluctuations in decaying grid turbulence. *Physical Review E* 64 (1), 016316.
- [10] Danaila, L., Voivenel, L., Varea, E., 2017. Self-similarity criteria in anisotropic flows with viscosity stratification. *Physics of Fluids* 29 (2), 020716.
- [11] Davidson, P. A., 2004. *Turbulence: An Introduction for Scientists and Engineers*. Oxford University Press.
- [12] Djenidi, L., Antonia, R. A., Danaila, L., 2017. Self-preservation relation to the kolmogorov similarity hypotheses. *Physical Review Fluids* 2 (5), 054606.
- [13] Frisch, U., 1995. *Turbulence - The legacy of A.N. Kolmogorov*. Cambridge University Press, Cambridge, UK.
- [14] Gauding, M., Danaila, L., Varea, E., 2017. High-order structure functions for passive scalar fed by a mean gradient. *International Journal of Heat and Fluid Flow* 67, 86–93.
- [15] Gauding, M., Dietzsch, F., Goebbert, J. H., Thévenin, D., Abdelsamie, A., Hasse, C., 2017. Dissipation element analysis of a turbulent non-premixed jet flame. *Physics of Fluids* 29 (8), 085103.

- [16] Gauding, M., Goebbert, J. H., Hasse, C., Peters, N., 2015. Line segments in homogeneous scalar turbulence. *Physics of Fluids* 27 (9), 095102.
- [17] George, W. K., 1992. The decay of homogeneous isotropic turbulence. *Physics of Fluids A: Fluid Dynamics* 4 (7), 1492–1509.
- [18] Goebbert, J. H., Gauding, M., Ansoerge, C., Hentschel, B., Kuhlen, T., Pitsch, H., 2016. Direct Numerical Simulation of Fluid Turbulence at Extreme Scale with psOpen. *Advances in Parallel Computing* 27, 777–785.
- [19] Goebbert, J. H., Iliev, H., Ansoerge, C., Pitsch, H., 2016. Overlapping of communication and computation in nb3dffft for 3d fast fourier transformations. In: *Juelich Aachen Research Alliance (JARA) High-Performance Computing Symposium*. Springer, pp. 151–159.
- [20] Gonzalez, M., Fall, A., 1998. The approach to self-preservation of scalar fluctuations decay in isotropic turbulence. *Physics of Fluids* 10 (3), 654–661.
- [21] Holzer, M., Siggia, E. D., 1994. Turbulent mixing of a passive scalar. *Physics of Fluids* 6 (5), 1820–1837.
- [22] Hou, T. Y., Li, R., 2007. Computing nearly singular solutions using pseudo-spectral methods. *Journal of Computational Physics* 226 (1), 379–397.
- [23] Ishida, T., Davidson, P., Kaneda, Y., 2006. On the decay of isotropic turbulence. *Journal of Fluid Mechanics* 564, 455–475.
- [24] Kolmogorov, A. N., 1941. Dissipation of energy in locally isotropic turbulence. In: *Dokl. Akad. Nauk SSSR*. Vol. 32. pp. 16–18.
- [25] Kolmogorov, A. N., 1941. The local structure of turbulence in incompressible viscous fluid for very large Reynolds numbers. In: *Dokl. Akad. Nauk SSSR*. Vol. 30. pp. 299–303.
- [26] Liepmann, H., 1949. Die Anwendung eines Satzes über die Nullstellen stochastischer Funktionen auf Turbulenzmessungen. *Helvetica Physica Acta* 22 (2), 119–126.
- [27] Mansour, N., Wray, A., 1994. Decay of isotropic turbulence at low Reynolds number. *Physics of Fluids* 6 (2), 808–814.

- [28] Meldi, M., Sagaut, P., 2013. Further insights into self-similarity and self-preservation in freely decaying isotropic turbulence. *Journal of Turbulence* 14 (8), 24–53.
- [29] Nelkin, M., 1994. Universality and scaling in fully developed turbulence. *Advances in physics* 43 (2), 143–181.
- [30] Obukhov, A., 1949. Temperature field structure in a turbulent flow. *Izv. Acad. Nauk SSSR Ser. Geog. Geofiz* 13, 58–69.
- [31] Pekurovsky, D., 2012. P3DFFT: a framework for parallel computations of Fourier transforms in three dimensions. *SIAM Journal on Scientific Computing* 34 (4), C192–C209.
- [32] Peters, N., Boschung, J., Gauding, M., Goebbert, J. H., Hill, R. J., Pitsch, H., 2016. Higher-order dissipation in the theory of homogeneous isotropic turbulence. *Journal of Fluid Mechanics* 803, 250–274.
- [33] Peters, N., Kerschgens, B., Paczko, G., 2013. Super-knock prediction using a refined theory of turbulence. *SAE International Journal of Engines* 6 (2), 953–967.
- [34] Pumir, A., 1994. A numerical study of the mixing of a passive scalar in three dimensions in the presence of a mean gradient. *Physics of Fluids* 6 (6), 2118–2132.
- [35] Rice, S. O., 1944. Mathematical analysis of random noise. *Bell Labs Technical Journal* 23 (3), 282–332.
- [36] Ristorcelli, J., 2003. The self-preserving decay of isotropic turbulence: Analytic solutions for energy and dissipation. *Physics of Fluids* 15 (10), 3248–3250.
- [37] Ristorcelli, J., 2006. Passive scalar mixing: Analytic study of time scale ratio, variance, and mix rate. *Physics of Fluids* 18 (7), 075101.
- [38] Rotta, J. C., 2010. *Turbulente Strömungen*. Vol. 8. Universitätsverlag Göttingen.
- [39] Schaefer, P., Gampert, M., Peters, N., 2012. On the scaling of the mean length of streamline segments in various turbulent flows. *Comptes Rendus Mécanique* 340 (11-12), 859–866.

- [40] Schaefer, P., Gampert, M., Wang, L., Peters, N., 2009. Fast and slow changes of the length of gradient trajectories in homogeneous shear turbulence. In: *Advances in Turbulence XII*. Springer, pp. 565–569.
- [41] Shraiman, B. I., Siggia, E. D., 2000. Scalar turbulence. *Nature* 405 (6787), 639–646.
- [42] Speziale, C. G., Bernard, P. S., 1992. The energy decay in self-preserving isotropic turbulence revisited. *Journal of Fluid Mechanics* 241, 645–667.
- [43] Sreenivasan, K., Prabhu, A., Narasimha, R., 1983. Zero-crossings in turbulent signals. *Journal of Fluid Mechanics* 137, 251–272.
- [44] Sreenivasan, K., Tavoularis, S., 1980. On the skewness of the temperature derivative in turbulent flows. *Journal of Fluid Mechanics* 101 (4), 783–795.
- [45] Sreenivasan, K. R., 1996. The passive scalar spectrum and the Obukhov–Corrsin constant. *Physics of Fluids* 8, 189.
- [46] Stephan, M., Docter, J., 2015. JUQUEEN: IBM Blue Gene/Q® supercomputer system at the Jülich supercomputing centre. *Journal of large-scale research facilities JLSRF* 1, 1.
- [47] Tang, S., Antonia, R., Djenidi, L., Danaïla, L., Zhou, Y., 2018. Reappraisal of the velocity derivative flatness factor in various turbulent flows. *Journal of Fluid Mechanics* 847, 244–265.
- [48] Tang, S., Antonia, R., Djenidi, L., Zhou, Y., 2016. Complete self-preservation along the axis of a circular cylinder far wake. *Journal of Fluid Mechanics* 786, 253–274.
- [49] Tong, C., Warhaft, Z., 1994. On passive scalar derivative statistics in grid turbulence. *Physics of Fluids* 6, 2165.
- [50] von Karman, T., Howarth, L., 1938. On the statistical theory of isotropic turbulence. *Proceedings of the Royal Society of London A: Mathematical, Physical and Engineering Sciences* 164 (917), 192–215.
- [51] Wang, L., 2008. Geometrical description of homogeneous shear turbulence using dissipation element analysis. Ph.D. thesis, RWTH-Aachen University.

- [52] Wang, L., 2009. Scaling of the two-point velocity difference along scalar gradient trajectories in fluid turbulence. *Physical Review E* 79 (4), 046325.
- [53] Wang, L., 2010. On properties of fluid turbulence along streamlines. *Journal of Fluid Mechanics* 648, 183–203.
- [54] Wang, L., 2014. Analysis of the lagrangian path structures in fluid turbulence. *Physics of Fluids* 26 (4), 045104.
- [55] Wang, L., Peters, N., 2006. The length-scale distribution function of the distance between extremal points in passive scalar turbulence. *Journal of Fluid Mechanics* 554, 457–475.
- [56] Wang, L., Peters, N., 2008. Length-scale distribution functions and conditional means for various fields in turbulence. *Journal of Fluid Mechanics* 608, 113–138.
- [57] Wang, L., Peters, N., 2013. A new view of flow topology and conditional statistics in turbulence. *Phil. Trans. R. Soc. A* 371 (1982), 20120169.
- [58] Warhaft, Z., 2000. Passive scalars in turbulent flows. *Annual Review of Fluid Mechanics* 32 (1), 203–240.
- [59] Yaglom, A., 1949. On the local structure of a temperature field in a turbulent flow. In: *Dokl. Akad. Nauk SSSR*. Vol. 69. pp. 743–746.
- [60] Zhou, T., Antonia, R. A., Danaïla, L., Anselmet, F., 2000. Transport equations for the mean energy and temperature dissipation rates in grid turbulence. *Experiments in Fluids* 28 (2), 143–151.